PAPER

Heterogeneous silicotungstic acid constructed *via* defect and morphology engineering for boosting the oxidative desulfurization of fuel oil†

Xiyang Zhou, [ID] [ab] Li Yu,[b] Xu Li,[b] Weizhou Jiao[b] and Ruixin Wang*[b]

It is well-known that defect engineering and morphology engineering are key strategies for giving an impetus to the catalytic activity of catalysts. This study reports the successful regulation of oxygen vacancy (O_V) defects and the morphology of a Keggin-type silicotungstic acid (SiW_{12})-loaded N-doped carbon (NC) matrix, which is obtained by calcining a copolymer of acryloyloxyethyl trimethyl ammonium chloride (DAC) and acrylamide (AM) as precursors in air. It was unveiled that adjusting the proportion of AM in the copolymer could be simultaneously conducive to the targeted regulation of O_V defects of catalysts and their morphological evolution from bowls to spheres. The as-prepared O_V-SiW_{12}/SNC sphere catalyst showed an excellent oxidative desulfurization (ODS) performance with H_2O_2 as a green oxidant. Complete removal of DBT (2000 ppm) was achieved within 12 minutes at 60 °C with a large rate constant of 0.4055 min^{-1}. The outstanding ODS performance was critically ascribed to the highly active W sites promoted by the abundant O_V defects, and the easy diffusion and contact between the substrate and W sites were led by the spherical structure. Moreover, the as-prepared catalyst exhibited prominent reusability. This ODS reaction was found to follow a HO• radical mechanism.

1. Introduction

Despite the continuous development of the new energy industry, crude oil remains the most commonly used energy source in most industries in the modern world.[1–3] However, fuel reserves continue to dwindle, leading to the use of low-quality fossil fuels containing a large amount of refractory sulfides, such as thiophene (Th), dibenzothiophene (DBT), benzothiophene (BT), 4,6-dimethyldibenzothiophenes (4,6-DMDBT), and other derivatives. The combustion of these sulfides could result in the release of sulfur oxides into air so as to the acid and smog, therefore posing serious threats to human health and ecosystems.[4–6] Moreover, thiophene compounds can poison catalysts used for automobile exhaust treatment and corrode refining equipment.[7] Currently, the limit for sulfur content in liquid fuels are becoming increasingly strict in various countries (even less than 60 ppb for organic sulfur compounds).[8] Therefore, it is urgent to develop highly efficient and feasible desulfurization techniques.

Although traditional hydrodesulfurization (HDS) has high efficiency for removing mercaptan, sulfide and disulfide from fuel feedstocks, it finds difficulty in removing refractory sulfides (such as DBT and its derivatives), and it requires harsh conditions (such as high temperature, high pressure, and substantial hydrogen consumption).[4] Recently, some non-hydrodesulfurization methods, including extractive desulfurization (EDS), adsorptive desulfurization (ADS), biological desulfurization (BDS), and oxidative desulfurization (ODS), have been developed to supplement HDS for the removal of refractory sulfides.[4,9,10] In particular, ODS is an attractive method with strong elimination ability for refractory sulfides under mild operating conditions, and hence, it is expected to produce ultra-clean fuels.[9,11] During ODS process, aromatic sulfur compounds are usually oxidized into sulfones, which could be then easily separated and recovered through adsorption, crystallization, rectification, extraction, and so on.[9,11–13]

A cost-effective and highly active catalyst is always a key factor for boosting the commercial viability of ODS technology.[1] To date, various catalysts, including polyoxometalates (POMs),[14,15] metal–organic frameworks (MOFs),[16,17] transition metal oxides (VO_x, WO_x, and MoO_x) or nitrides (W_2N and Mo_2N),[1,18–21] transition metal carbides (Mo_2C and W_2C),[22,23] and transition metals (Co),[24] have been widely explored for ODS of fuel oil. Among them, POMs, as a class of metal–oxygen clusters consisting of early transition metals (W, V, Mo, *etc.*) in their high oxidation states, have received significant attention as effective catalysts owing to their appealing properties, such as their particular structure, excellent redox activity, good stability, and mild reaction conditions.[25,26] Notably, the heterogeneous POMs with SiO_2,

ᵃDepartment of Chemical and Material Engineering, Lyuliang University, Lv Liang, Shanxi 033001, China. E-mail: 20111013@llu.edu.cn; Fax: +86-351-3921497; Tel: +86-18234838896

ᵇSchool of Chemistry and Chemical Engineering, North University of China, Taiyuan, Shanxi 030051, China. E-mail: zbdxwrx@nuc.edu.cn; zbdxjwz@nuc.edu.cn

porous carbon materials, and MOFs as supports, are atttracting increasingly widespread interest owing to more exposed active sites triggered by the good distribution of active components.[27,28] Morphology engineering is always a good strategy for improving the catalytic activity of catalysts. Generally, the spherical shape has the advantages of good fluidity and high specific surface area, which makes it easier for reactant molecules to come into contact with the active center, thus exhibiting an excellent catalytic effect.[27,29] Furthermore, defect engineering has been found to be promising for greatly improving the performance of catalysts.[5,30–33] Typically, the oxygen vacancy (O_V) defect can generate favorable effects for regulating the surface-electron state and boosting the redox reaction (such as the oxidative desulfurization reaction).[5] Ma et al.[34] synthesized an O_V-defective catalyst, $H_4PVMo_4W_7O_{40}$@rht-MOF-1-De, using a one-pot method for fuel oil desulfurization. It exhibited high catalytic activity and recyclability, achieving 99% DBT and 96% 4,6-DMDBT removal under optimized conditions. In the context of oxidative desulfurization (ODS) reactions, Jiao et al.[1] discovered that the presence of oxygen vacancies significantly promoted the generation of active intermediates, thereby enhancing the overall rate of the ODS reaction. This observation underscores the crucial role of oxygen vacancies in facilitating efficient sulfur removal.

Herein, a novel strategy for effectively modulating oxygen vacancy (O_V) defects and the morphology of a Keggin-type silicotungstic acid (SiW_{12})-loaded N-doped carbon (NC) matrix is developed by adjusting the content of acrylamide (AM) in a copolymer of acryloyloxyethyl trimethyl ammonium chloride (DAC) and acrylamide (AM) (abbreviated as CPAD) as precursors. Finally, by in situ low-temperature calcination of CPAD in air, a spherical catalyst with abundant O_V defects (O_V-SiW_{12}/SNC) was successfully prepared and applied to the deep ODS of fuel oil. The as-prepared O_V-SiW_{12}/SNC catalyst shows an excellent oxidative desulfurization (ODS) performance, wonderful adaptability to fuel oils with a wide range of sulfur concentrations, and remarkable reusability. In addition, a series of radical scavenging studies were performed to elucidate the ODS mechanism of O_V-SiW_{12}/SNC.

2. Experimental

2.1. Materials

Acrylamide (AM, AR, C_3H_5NO, Tianjin Dengfeng Chemical Reagent Factory); acryloyloxyethyl trimethyl ammonium chloride (DAC, 80 wt% in H_2O, $C_8H_{16}ClNO_2$, Shanghai Maclean Biochemical Technology Co., Ltd); silicotungstic acid (H_4-$SiW_{12}O_{40}·xH_2O$, abbreviated as SiW_{12}, AR, Shanghai Maclean Biochemical Technology Co., Ltd); dibenzothiophene (DBT, ≥99%, $C_{12}H_8S$, Aladdin); 4,6-dimethyldibenzothiophene (4,6-DMDBT) (97%, $C_{14}H_{12}S$, Aladdin); thiophene (BT, 99%, C_4H_4S); n-octane (AR, Tianjin Damao Chemical Reagent Factory); H_2O_2 aqueous solution (AR, 30 wt%, Tianjin Damao Chemical Reagent Factory); and acetonitrile (AR, CH_3CN, Tianjin Concord Technology Co., Ltd). All the other chemicals and reagents are commercially available and analytically pure (see Section 1 in the (ESI)† for more details).

2.2. Preparation of catalysts

First, copolymerized crosslinked microspheres (CPAD) of acrylamide (AM) and acryloyloxyethyl trimethyl ammonium chloride (DAC) were prepared by applying the reverse suspension polymerization method (see Section 2 of the (ESI)† for more details). Then, a certain amount of silicotungstic acid (SiW_{12}) can be combined with CPAD through the electrostatic interaction to produce the spherical precursor SiW_{12}/CPAD (Fig. S1†). Finally, SiW_{12}/CPAD is calcined at different temperatures to obtain spherical catalysts, i.e. SiW_{12}/CPAD-300, SiW_{12}/CPAD-400, SiW_{12}/CPAD-500, and SiW_{12}/CPAD-700, where the numbers represent calcination temperatures. Importantly, during the synthesis process, the feed ratio of DAC and AM is explored in the range of 4 : 0–4 : 3 to regulate the morphology of the final calcination products. Unless otherwise specified, the DAC/AM feed ratio is determined to be 4 : 2, and the corresponding precursor and spherical SiW_{12}/CPAD-400 product are denoted as SiW_{12}/CPAD and O_V-SiW_{12}/SNC, respectively. Besides, to highlight O_V-SiW_{12}/SNC, the obtained calcinating products of pure SiW_{12} and the SiW_{12}/CPAD precursor with a feed molar ratio of DAC to AM of 4 : 0 at 400 °C are marked as SiW_{12}-400 and SiW_{12}/NC, respectively. The preparation process of O_V-SiW_{12}/SNC is schematically shown in Fig. 1, and the molecular structures of DAC, AM, MBA, and CPAD are depicted in Fig. S2.†

2.3. Characterizations

Fourier Infrared Spectrometer (FT-IR, KBr method, L1600300 Spectrum Two Lita Model, Liantrisant, UK); UV-Visible Spectrophotometer (UV-Vis, UV-2802, Unico, China); High
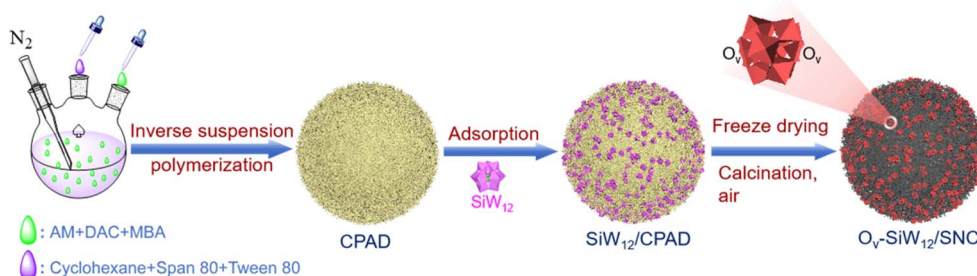

Fig. 1 Preparation process of O_V-SiW_{12}/SNC.

Performance Liquid Chromatograph (HPLC, Model Classical 3100, Dalian Yi lite Analytical Instrument Co., Ltd, Dalian, China); element analyser (EA, PE2400 Series II CHNS/O type, Qingdao Huaqing Group Co., Ltd China); and a Powder X-ray diffractometer (XRD, Empyrean, PANalytical B.V., Holland, Cu K(α) radiation ($\lambda = 1.5418$ Å, 40 kV and 40 mA) over a range of $2\theta = 5$–$90°$). Electron paramagnetic resonance spectroscopy (EPR) was performed using a MiniScope MS 5000 spectrometer (Magnettech, Germany) in the dark at room temperature. Scanning electron microscopy (SEM, Zeiss Merlin Compact, Germany); X-ray photoelectron spectroscopy (XPS, Thermo Scientific K-Alpha+, USA); Synchronous thermal analysis (TG-DSC, LF-1100, Mettler Toledo Instruments Co., Ltd, Shanghai, China, air atmosphere, a heating rate of 5 °C min^{-1}); and High-performance liquid chromatography (HPLC, EClassical 3100, Dalian Yilite Analytical Instrument Co., Ltd, Dalian, China). Inductively coupled plasma optical emission spectrometry (ICP-OES, Agilent 5110, USA) was used to determine the W content.

2.4. ODS experiments

First, the model oil with a sulfur content of 500–4000 ppm (parts per million by weight) was produced by dissolving DBT (or BT, 4,6-DMDBT) into *n*-octane. The extraction-catalyzed ODS reaction was carried out in a two-phase system consisting of model oil and acetonitrile. Specifically, 20 mL of the model oil and 20 mL of acetonitrile were mixed and stirred at the reaction temperature for 20 min to achieve extraction equilibrium. Subsequently, an ODS reaction occurred, followed by the addition of O_V-SiW$_{12}$/SNC and 30 wt% of H$_2$O$_2$ aqueous solution with a certain H$_2$O$_2$/sulfur (O/S) molar ratio into the above two-phase system. During the reaction, trace samples were periodically removed from the two phases and then diluted with *n*-octane and acetonitrile to detect the residual sulfur concentration by employing the HPLC external standard method (see Section 3 of the ESI† for details). At the end of the reaction, the catalyst was collected, washed with acetonitrile and ethanol, dried at 50 °C, and then recovered for reuse.

3. Results and discussion

3.1. Characteristics of catalysts

The morphology of the calcination products with the feed ratios of DAC and AM in the range of 4 : 0–4 : 3 at 400 °C was observed by SEM. As displayed in Fig. 2(a–c) and S3,† with the feed DAC/AM ratio in the range of 4 : 0–4 : 3 during the preparation of precursors, the morphology of the calcination products varies from bowl shape with thin walls to the bowl with increased wall thickness and then to spherical structure, which may be related to the thermal decomposition of CPAD microspheres. Herein, the feed DAC/AM ratio is determined to be 4 : 2 to guarantee the spherical O_V-SiW$_{12}$/SNC catalyst. Moreover, the EDX element mapping in Fig. 2(d) shows that the C, N, O, Si, and W elements are evenly distributed in the O_V-SiW$_{12}$/SNC microspheres,
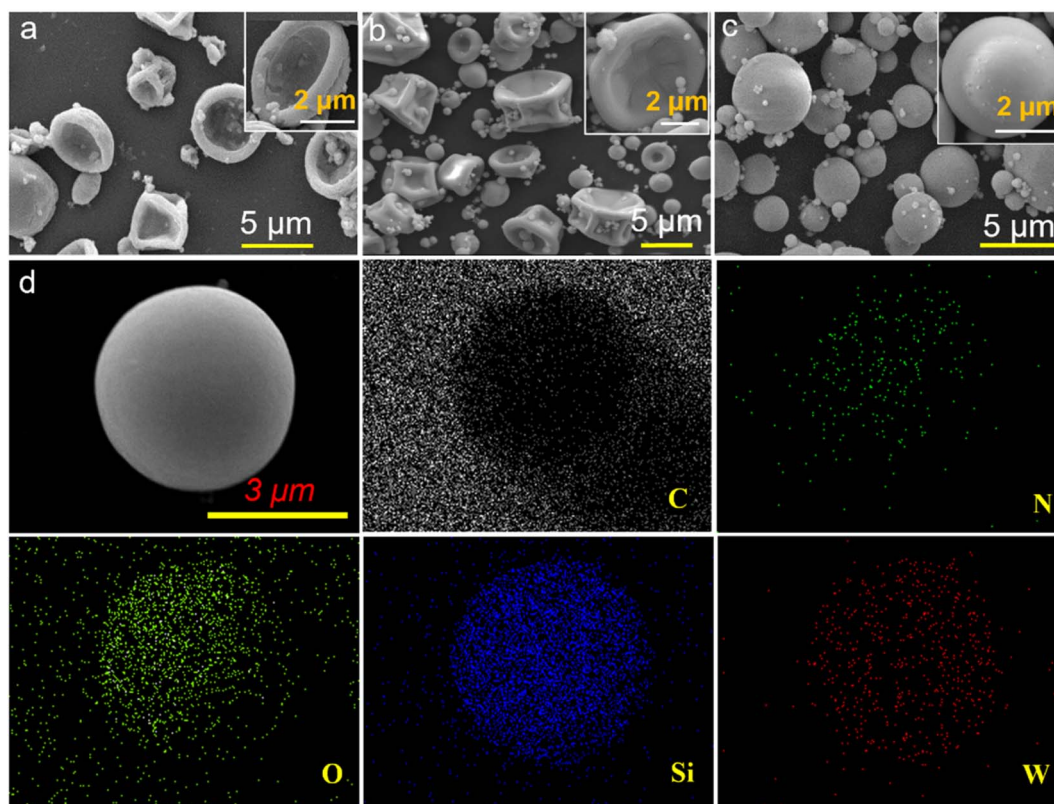

Fig. 2 SEM images of O_V-SiW$_{12}$/SNC derived from different DAC/AM feed molar ratios of (a) 4 : 0, (b) 4 : 1, (c) 4 : 2 and (d) HADDF and EDX elemental mapping images of O_V-SiW$_{12}$/SNC.
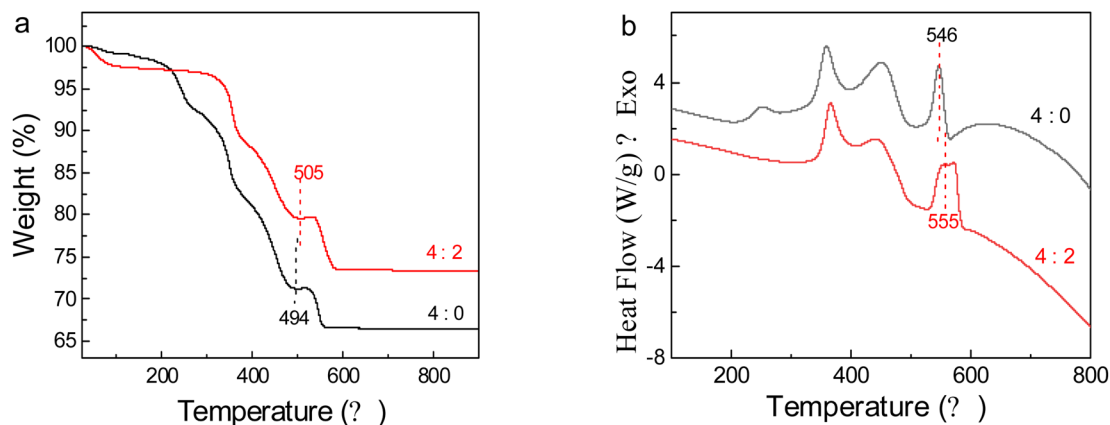
Fig. 3 (a) TG and (b) DSC curves of precursors SiW$_{12}$/CPAD with feed DAC/AM molar ratios of 4 : 0 and 4 : 2 (in air).

indicating the even distribution of O$_V$-SiW$_{12}$ in the spherical NC matrix. Furthermore, the SiW$_{12}$/CPAD precursors with different DAC/AM feed molar ratios of 4 : 2 and 4 : 0 present similar TG and DSC curves (Fig. 3), in which the precursor with a DAC/AM feed molar ratio of 4 : 0 is named SiW$_{12}$/CPAD-0. The TG curves of SiW$_{12}$/CPAD show four distinct weight loss stages. The weight loss below 280 °C is owing to the removal of physically and chemically adsorbed water and decomposition of MBA in CPAD; the weight loss at 280–400 °C with an exothermic peak at 365 °C is ascribed to the damage of the quaternary ammonium group[35,36] and the loss of crystal water in H$_4$SiW$_{12}$O$_{40}$·xH$_2$O;[27] the weight loss at 400–505 °C along with an exothermic peak at 441 °C is attributed to the combustion of residual carbon skeleton and the deprotonation of H$_4$SiW$_{12}$O$_{40}$ into SiW$_{12}$O$_{38}$,[27,35,37] which can be further demonstrated by the color of products at 400 and 500 °C (Fig. S4a†); the weight loss at 506–600 °C along with two exothermic peaks at 555 °C and 572 °C is accredited to the transformation of SiW$_{12}$ to silicon- and tungsten-oxides.[38,39] Compared to the TG and DSC curves of the SiW$_{12}$/CPAD-0 precursor, it is depicted that the thermo-decomposed temperatures of the SiW$_{12}$/CPAD precursor in each pyrolysis stage increase owing to the addition of AM, which could also be unmasked by comparing their colors at 300–500 °C (Fig. S4†). Therefore, when the temperature increases to 400 °C, the residual weight of SiW$_{12}$/CPAD (87.9%) is greater than that of SiW$_{12}$/CPAD-0 (80.8%) (Fig. 3a), which favors better preservation of the spherical carbon skeleton after calcining SiW$_{12}$/CPAD.

The FT-IR spectrum of the CPAD (Fig. S5†) shows that not only the characteristic absorption peaks of DAC (at 1164 cm^{-1}, 1479 cm^{-1} and 1740 cm^{-1} corresponding to the stretching vibration of C–O, –CH$_2$–N$^+$ and C=O, respectively)[40] but also those of AM (at 1667 cm^{-1} corresponding to the stretching vibration of –NH$_2$) appear,[41] confirming the formation of the copolymerized crosslinked microspheres CPAD. In the FT-IR spectrum of SiW$_{12}$/CPAD, in addition to peaks of CPAD, the characteristic absorption peaks of SiW$_{12}$ are found at 1017, 973, 920, 881 and 796 cm^{-1} ascribed to the stretching vibration of Si–O$_a$, W–O$_d$, W–O$_b$–W, O–O and W–O$_c$–W bonds, respectively,[42,43] verifying the successful combination of SiW$_{12}$ onto CPAD.

Fig. 4a illustrates the FT-IR spectra of the calcination products of SiW$_{12}$/CPAD at different temperatures. When calcinating at 300 °C, the peaks of SiW$_{12}$ remain basically unchanged, but the peak of AM in CPAD at 1667 cm^{-1} is greatly reduced, suggesting that the structure of CPAD has changed. After calcinating SiW$_{12}$/CPAD at 400 °C, the peaks assigned to AM and DAC in CPAD have almost gone, and the peaks of SiW$_{12}$ at 1017, 973, 920, and 796 cm^{-1} remain basically the same except for the peak at 880 cm^{-1} corresponding to the O–O bond that almost disappears, indicating that not only the structure of CPAD is destroyed owing to carbonization (see the blackened product shown in Fig. S4†), but also that of SiW$_{12}$ is damaged to some extent owing to the formation of oxygen vacancies, which is further supported by the presented symmetric peak at $g = 2.003$ in the electron paramagnetic resonance (EPR) spectrum compared with the SiW$_{12}$/CPAD precursor and its calcined product at 300 °C (Fig. S6†). As the calcination temperature exceeds 500 °C, the peaks of both CPAD and SiW$_{12}$ disappear completely, and only a large, wide peak appears at about 790 cm^{-1} corresponding to the W–O–W bond.[27] This significant structural change is also disclosed by XRD patterns. As shown in Fig. 4b, the calcination products at 400 and 300 °C exhibit XRD patterns similar to that of the SiW$_{12}$/CPAD precursor, with almost no diffraction peaks, indicating the uniform dispersion of SiW$_{12}$ in the CPAD matrix or its derived carbon materials[39,44,45] and the preservation of the basic SiW$_{12}$ structure even after calcination at 300 or 400 °C in air, which agrees with the literature.[5,27] However, as the calcination temperature exceeds 500 °C, the XRD patterns of the calcination products are distinctly different, and some clear diffraction peaks appear, corresponding to the monochromatic WO$_3$ phase (PDF # 71-0131), which comes from the oxidation and decomposition of SiW$_{12}$. The XRD results are in good agreement with those of the FT-IR spectra. To sum up, the calcination temperature of 400 °C is indispensable for ensuring the basic structure of SiW$_{12}$ while creating partial oxygen vacancy defects.

Furthermore, X-ray photoelectron spectroscopy (XPS) was performed to evaluate the chemical environment and composition of O$_V$-SiW$_{12}$/SNC, as shown in Fig. 4c and S7.† The XPS survey spectrum (Fig. S7a†) shows the presence of C, O, N, W,
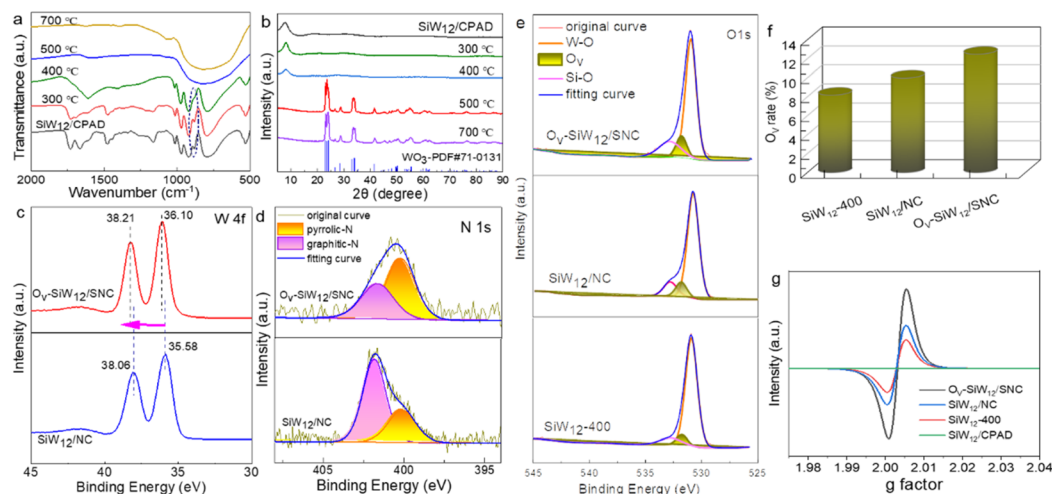
Fig. 4 (a) FT-IR spectra and (b) XRD patterns of SiW$_{12}$/CPAD, and its annealing products at different temperatures. High resolution XPS spectra of (c) W 4f and (d) N 1s. (e) High resolution XPS spectra of O 1s in the specimens. (f) Proportions of O vacancies for three specimens deduced from (e) and (g) EPR spectra of the specimens.

and Si elements in accordance with the EDX element mapping results. In the high resolution W 4f spectrum of O$_V$-SiW$_{12}$/SNC (Fig. 4c), two split peaks at 36.10 and 38.21 eV respectively correspond to W^{6+} of SiW$_{12}$,[5] and are redshifted compared to SiW$_{12}$/NC, suggesting that the electronic structure of W elements changes. In addition, it is clearly found in the N 1s spectra of O$_V$-SiW$_{12}$/SNC and SiW$_{12}$/NC (Fig. 4d) that two peaks at 400.1 and 401.8 eV are ascribed to pyrrolic N and graphitic N, respectively,[46] and the ratio of pyrrolic N to graphitic N for O$_V$-SiW$_{12}$/SNC is notably greater than that for SiW$_{12}$/NC. The coordination of pyrrolic N with metal (W) atoms can regulate its electronic structure and thus promote its catalytic activity.[47] Hence, a higher ratio of pyrrolic N to graphitic N for O$_V$-SiW$_{12}$/SNC is propitious to facilitate its catalytic activities. The O 1s spectrum (Fig. 4e) can be fitted into three peaks at 530.9 eV, 531.8 eV and 532.8 eV, corresponding to the W–O, O$_v$, and Si–O bonds, respectively.[48,49] Importantly, it can be found from Fig. 4e and f that the O$_V$ contents of various specimens decrease in the order O$_V$-SiW$_{12}$/SNC > SiW$_{12}$/NC > SiW$_{12}$-400, which is also verified by changes in the intensity of signal peaks of O$_V$ defects at $g = 2.003$ observed in the EPR spectrum depicted in Fig. 4g. Therefore, the addition of AM to the precursor facilitates the formation of more O$_V$ defects, which could modulate the electronic structure of the active W sites in SiW$_{12}$, thus accelerating the decomposition of H$_2$O$_2$ and improving the ODS performance of O$_V$-SiW$_{12}$/SNC.

3.2. ODS performance evaluation

3.2.1 ODS performances of different catalytic systems. The ODS performance of the different reaction systems is shown in Fig. 5a. It can be observed from Fig. 5a that the catalyst and H$_2$O$_2$ are essential in the extraction–oxidation desulfurization model. Concurrently, in the absence of H$_2$O$_2$, O$_V$-SiW$_{12}$/SNC shows an adsorption capacity of about 8.96 mg g^{-1} towards DBT. Notably, it is still found that in the presence of H$_2$O$_2$, the ODS performance of catalysts follows the order O$_V$-SiW$_{12}$/SNC >

SiW$_{12}$-400 > pure SiW$_{12}$. According to Fig. S8a,† SiW$_{12}$-400 possesses an XRD pattern similar to that of pure SiW$_{12}$, indicating that they have almost the same structure. Moreover, SiW$_{12}$-400 exhibits O$_V$ defects owing to calcination, but there are no O$_V$ defects in pure SiW$_{12}$ (Fig. S8b†), demonstrating that SiW$_{12}$-400 has a higher desulfurization rate than pure SiW$_{12}$. Thus, O$_V$-SiW$_{12}$/SNC presents better ODS performance than SiW$_{12}$-400, which is related not only to the excellent dispersion of SiW$_{12}$ in the N-doped carbon matrix and the uniform suspension of O$_V$-SiW$_{12}$/SNC in the acetonitrile phase (Fig. S9†) but also to more O$_V$ defects of O$_V$-SiW$_{12}$/SNC than that of SiW$_{12}$-400 (Fig. 4g).

Furthermore, it is surprising to find that with the feed DAC/AM ratio in the range of 4:0–4:3 during the preparation of precursors, not only the morphology of the corresponding calcined products varies from bowl shape to spherical structure (as shown in Fig. S3†), but also the O$_V$ defects of calcined products increase until the precursor with the feed DAC/AM ratio of 4:2 produces the almost same number of O$_V$ defects as that with 4:3 (Fig. 5b). Accordingly, with the addition of AM, fuel oil achieves ultra-deep desulfurization in a short time with a lower O/S ratio (3:1). Moreover, with the increased feed amount of AM, the feed DAC/AM ratio was stretched up in the range of 4:0–4:3, and the ODS performance of the corresponding calcined products becomes better and better owing to the fast mass transfer process supported by the spherical morphology, more O$_V$ defects induced by the introduction of AM, and the modulated electronic structure of W active sites by O$_V$ defects (Fig. 4c). In view of almost the same desulfurization ratio of the sample with a feed DAC/AM ratio of 4:2 as that with 4:3, the feed DAC/AM ratio is optimized as 4:2.

In addition, the ODS performances of the calcinated products of the precursor SiW$_{12}$/CPAD with a DAC/AM feed molar ratio of 4:2 at different temperatures are explored to uncover the particularity of the calcination temperature of 400 °C, as shown in Fig. 5d. It is clear that too high or too low a calcination
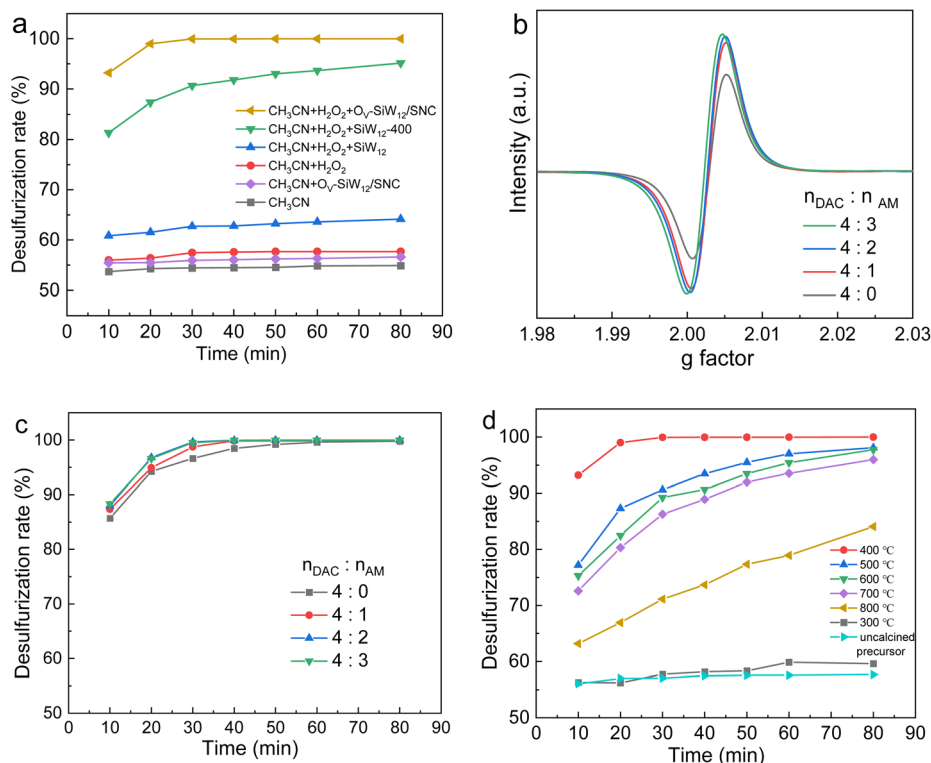
Fig. 5 ODS performances of (a) different reaction systems. (b) EPR tests and ODS performances for the calcined products (c) with different ratios of DAC to AM (calcination condition: 400 °C), and (d) at different temperatures (ODS conditions: DBT content: 500 ppm; catalysts: 0.1 g; $n(H_2O_2) : n(S) = 3 : 1$; $T = 60$ °C).

temperature is not conducive to the ODS performance of the calcinated products. Combined with FT-IR, XRD, and EPR results (Fig. 4a, b, and S6†), the structure of SiW_{12} in the calcined product at 300 °C is the same as that in the precursor, with no O_V defects, thus demonstrating a lower ODS activity. Although the Keggin structure of SiW_{12} in the calcined product at 400 °C is maintained, more O_V defects appear (Fig. S6†), resulting in excellent ODS activity. As the calcination temperature increases beyond 400 °C, the desulfurization rate decreases instead, which is related to the structural transformation of SiW_{12} into WO_3 (Fig. 4b). The reduction of exposed active sites

led to the aggregation of WO_3 species owing to the loss of carbon layers as a barrier during high temperature calcination (as shown in the TG result in Fig. 3a).

3.2.2 Effects of various factors on ODS performance. It is well known that the catalyst dosage, the molar ratio of H_2O_2 to sulfur compounds (O/S), and the reaction temperature are usually the key parameters for the ODS reaction. Therefore, they were investigated to optimize the ODS reaction. As illustrated in Fig. S10† and elucidated by the corresponding discussion, the optimal catalyst dosage and the molar ratio of $n(H_2O_2)$ to $n(S)$ are determined to be 0.2 g and 4 : 1, respectively.
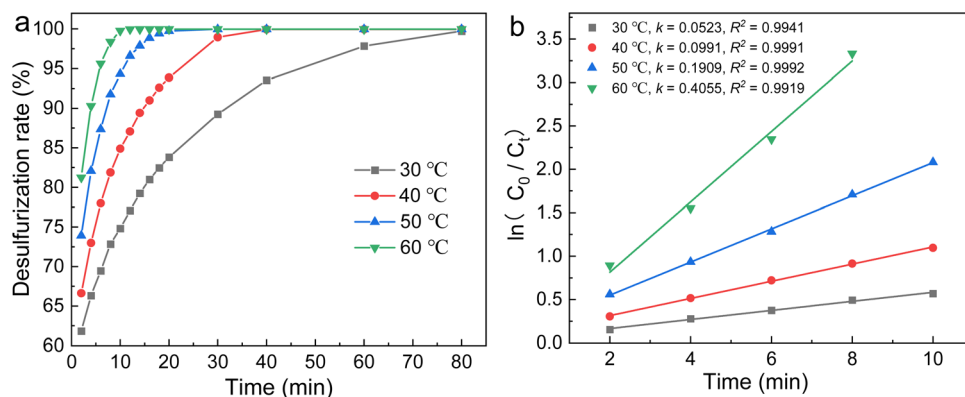

Fig. 6 (a) ODS efficiencies at different reaction temperatures and (b) pseudo-first-order kinetic curves (DBT content: 2000 ppm; catalysts: 0.2 g; $n(H_2O_2) : n(S) = 4 : 1$).

Table 1 Comparison of different ODS systems in the presence of H_2O_2

Catalyst	Reaction conditions	Time	Desulfurization rate	Ref.
HPW@UiO-66	800 ppm, 0.08 g catalysts, 20 mL mode oil, O/S = 7, T = 60 °C	90 min	100%	50
WOx@mSnO$_2$	500 ppm, 0.1 g catalysts, 20 mL mode oil, O/S = 5, T = 60 °C	120 min	100%	51
[mim(CH$_2$)$_3$COO]$_3$PW@UiO-66	1000 ppm, 0.16 g catalysts, 20 mL mode oil, O/S = 5, T = 70 °C	60 min	100%	44
30HPW/ZrO$_2$	500 ppm, 0.1 g catalysts, 20 mL mode oil, O/S = 4, T = 60 °C	120 min	100%	52
HPW-vim	500 ppm, 0.20 g catalysts, 20 mL mode oil, O/S = 5, T = 50 °C	30 min	100%	53
CeO$_2$-WO$_x$-TiO$_2$	1154 ppm, 0.20 g catalysts, 100 mL mode oil, T = 60 °C	30 min	98%	54
O$_V$-SiW$_{12}$/SNC	**2000 ppm, 0.2 g catalysts, 20 mL mode oil, O/S = 4, T = 60 °C**	**12 min**	**100%**	**This work**

Generally, the reaction temperature plays a dominant role in improving ODS efficiency. As illustrated in Fig. 6a, the desulfurization efficiency of O$_V$-SiW$_{12}$/SNC is substantially improved with an increased temperature, which is ascribed to the facilitated probability of collision between the reactants, oxidants, and catalysts, and hence the promoted reaction rate. Optimally, it reaches 100% of DBT removal from the 2000 ppm of model fuel within 12 minutes at 60 °C, better than most reports (Table 1). Surprisingly, even at lower temperatures, the DBT removal rate was still up to 100% within 40 min (at 40 °C) and 99.7% within 80 min (at 30 °C), indicating the outstanding ODS activity of O$_V$-SiW$_{12}$/SNC. Furthermore, the kinetic plots for ODS reactions over the catalyst are performed, as shown in Fig. 6b (see Section 4 of ESI† for the fitting method). These results demonstrate that all of them follow the pseudo-first-order kinetic model, as confirmed by the high correlation factor (R^2 > 0.99). When the reaction temperature is 60 °C, the rate constant is as high as 0.4055 min^{-1}.

Additionally, the O$_V$-SiW$_{12}$/SNC catalyst achieves a turnover frequency (TOF) value of 10.65 h^{-1} at 60 °C by utilizing the W atom as the active site based on a W content of 2.93 mmol g^{-1} calculated by the ICP-OES test according to Formula (S2) in the ESI.† Notably, the TOF value of the spherical O$_V$-SiW$_{12}$/SNC catalyst with more O$_V$ defects is about 10 times that (1.39 h^{-1}) of the bowl SiW$_{12}$/NC catalyst with less O$_V$ defects obtained by the corresponding precursor with no addition of AM,[5] verifying the

great advantage of introducing AM components into the precursor once again.

3.2.3 Investigation on the desulfurization adaptability of O$_V$-SiW$_{12}$/SNC. To evaluate the industrial adaptability of the as-prepared O$_V$-SiW$_{12}$/SNC catalyst, ODS performances of various fuel oils with different S contents (500∼4000 ppm) and different sulfur compounds (DBT, 4,6-DMDBT, and BT) are studied. As shown in Fig. 7a, the desulfurization efficiency of fuel oils containing different sulfur compounds follows the order DBT>4,6-dmdbt > BT depending on the electron density of the sulfur (S) atom and the steric hindrance, which is consistent with the literature.[1,27,55,56] Among them, a higher electron density of the sulfur (S) atom of DBT (5.758) than that of BT (5.739) makes the former more vulnerable to electrophilic attack by reactive oxygen species, thus expediting the oxidation of DBT.[57] However, 4,6-DMDBT with the highest electron density (5.760) of the S atom presents slightly weaker ODS performance than DBT, attributed to the synergistic effect of greater steric hindrance caused by two methyl groups on the benzene ring and the greatest electron density of the S atom. Fig. 7b presents the desulfurization efficiency of fuel oils with S contents in the range of 500–2000 ppm. It is distinctly observed that the O$_V$-SiW$_{12}$/SNC catalyst could eliminate DBT from model oils with a wide range of S contents (500–4000 ppm) within 10–30 min, suggesting again that the O$_V$-SiW$_{12}$/SNC catalyst can be a promising potential catalyst for the ODS reaction of fuel oil.
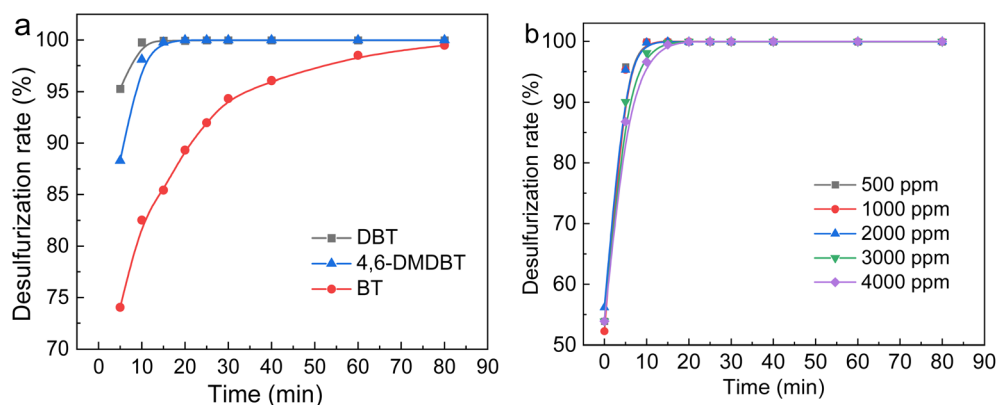

Fig. 7 ODS performances of model oil with different sulfur compounds (DBT, 4,6-DMDBT, and BT) (a) and different sulfur contents (500–4000 ppm) (b) (catalyst: 0.2 g; $n(H_2O_2)$: $n(S)$ = 4 : 1; T = 60 °C).
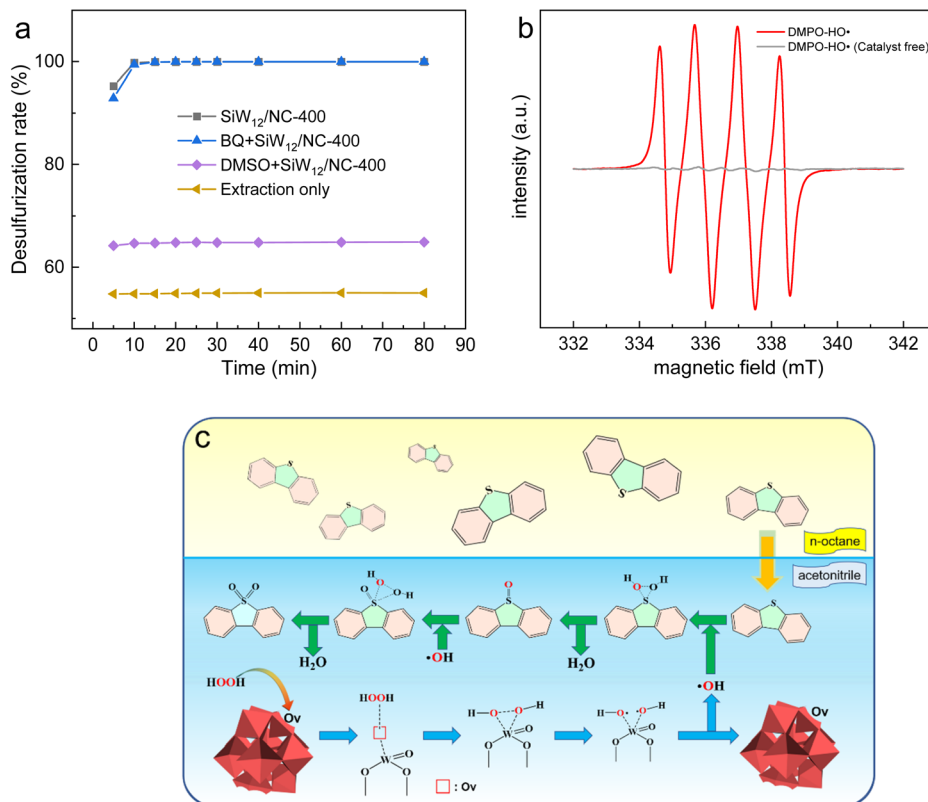
Fig. 8 (a) Removal efficiency of DBT in the presence of scavengers. (b) EPR spectrum of the reaction system. (c) Mechanism diagram of the ODS reaction over O_V-SiW$_{12}$/SNC (catalyst: 0.2 g; $n(H_2O_2):n(S) = 4:1$; $T = 60$ °C).

3.2.4 ODS reaction mechanism. Usually, *p*-benzoquinone (BQ) and dimethyl sulfoxide (DMSO) are used as quenchers for superoxide anion radical ($O_2^{\cdot-}$) and hydroxyl radical ($HO^{\cdot}$), respectively,[23] to elucidate the ODS mechanism of O_V-SiW$_{12}$/SNC. As shown in Fig. 8a, BQ slightly affects ODS efficiency, demonstrating the absence of $O_2^{\cdot-}$ radical in the ODS reaction. However, the addition of DMSO can greatly inhibit the desulfurization efficiency, indicating that the $HO^{\cdot}$ radical plays an essential role in the ODS reaction. In addition, the electron paramagnetic resonance (EPR) spectrum (Fig. 8b) using 5, 5-dimethylpyrroline-oxide (DMPO) as a radical scavenger shows a fourfold peak with a peak area ratio of 1:2:2:1, confirming the presence of the $HO^{\cdot}$ radical and thus a free radical reaction mechanism for the ODS reaction, which is similar to the results in the literature.[5,29]

Furthermore, Fig. S11† shows HPLC chromatograms of the *n*-octane and acetonitrile phases during the ODS reaction. As the ODS reaction proceeds, DBT in the acetonitrile phase is initially oxidized into DBTO and eventually into DBTO$_2$. Combined with the aforementioned results, the possible reaction mechanism (Fig. 8c) is inferred as follows. DBT is first transferred from the *n*-octane phase to the acetonitrile phase. Simultaneously, in the acetonitrile phase, H_2O_2 is activated by O_V-SiW$_{12}$/SNC to generate $HO^{\cdot}$; then, DBT is oxidized by $HO^{\cdot}$ into DBTO and further into DBTO$_2$. During the key process, not only the W active sites with high electron density triggered by O_V defects boost the cleavage of O–O bonds of H_2O_2 and thus the

generation of a substantial quantity of electrophilic $HO^{\cdot}$ species,[58] but also the spherical structure of O_V-SiW$_{12}$/SNC is conducive to the exposure of W active sites and the diffusion of DBT and H_2O_2, thereby providing opportunities for excellent interaction with active species and reactants, which thus facilitates the ODS reaction. With the transformation of DBT in the acetonitrile phase into DBTO and DBTO$_2$, the extraction equilibrium is disturbed, and the residual DBT in the *n*-octane phase is further extracted into the acetonitrile phase for the subsequent oxidation reaction. In this way, extraction and oxidation are carried out alternately until all DBTs are completely transferred from the *n*-octane phase into the acetonitrile phase and converted into DBTO$_2$ in the acetonitrile phase, thereby obtaining the final complete removal of DBT from the *n*-octane phase.

3.2.5 Reusability of O_V-SiW$_{12}$/SNC. The reusability of O_V-SiW$_{12}$/SNC is evaluated, as shown in Fig. 9a. It is clear that after 6 cycles, the desulfurization rate can still reach 100%, and only the complete desulfurization time is slightly extended. In addition, it can be observed from the filtration experiment depicted in Fig. S12† that DBT is no longer removed after O_V-SiW$_{12}$/SNC is filtered out, indicating its good stability. The structural stability of O_V-SiW$_{12}$/SNC can also be verified by comparing the XRD patterns (Fig. 9b) and FT-IR spectra (Fig. 9c) of fresh and recovered catalysts. As illustrated in Fig. 9b and c, the structure of the recovered catalyst does not show significant changes compared to that of the fresh one, and only two weak
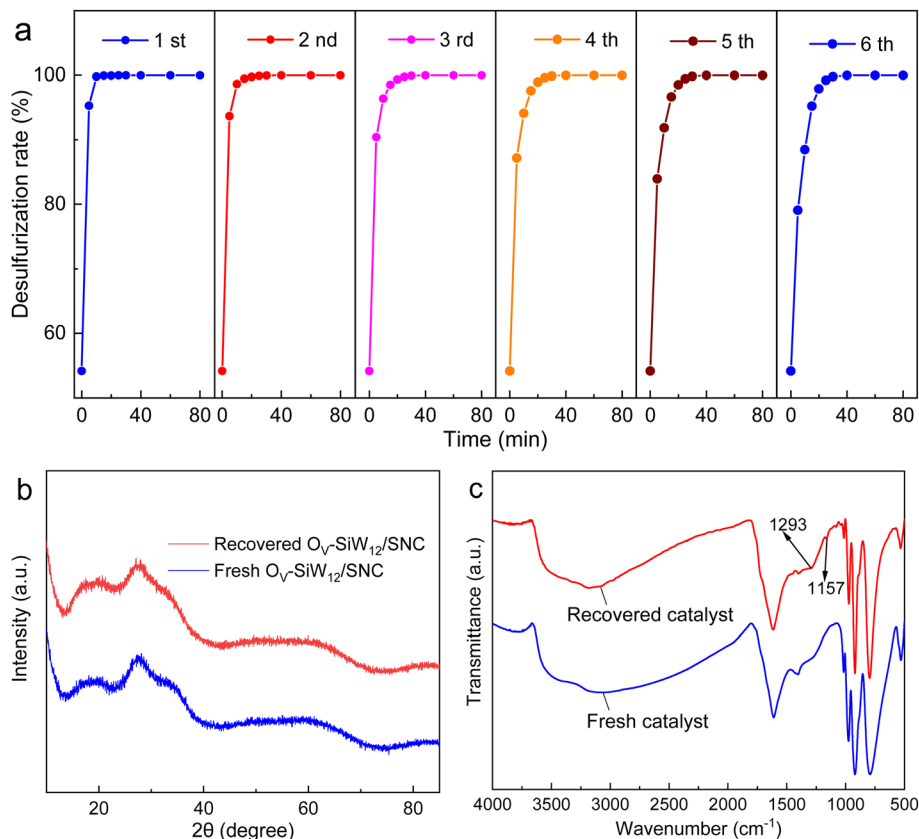
Fig. 9 (a) Reusability of the catalyst. (b) XRD patterns and (c) FT-IR spectra of fresh and recovered catalysts.

absorption peaks appear at 1293 cm^{-1} and 1157 cm^{-1} in the FT-IR spectrum of the recovered catalyst, which can be attributed to the asymmetric and symmetrical tensile vibrations of the O=S=O bond of DBTO$_2$.[5,58]

4. Conclusion

In conclusion, the spherical O$_V$-SiW$_{12}$/SNC catalyst with abundant O$_V$ defects was successfully synthesized through *in situ* low-temperature calcination of the copolymer of AM and DAC as a precursor in air for deep ODS of fuel oil. It is depicted that during the preparation, the introduction of AM in the precursor could facilitate the formation of more O$_V$ defects and the evolution of the morphology from bowl to sphere. The as-prepared O$_V$-SiW$_{12}$/SNC catalyst exhibits an excellent ODS activity and outstanding reusability. It could effectively eliminate DBT from fuel oil with a sulfur content of 2000 ppm within 12 minutes at 60 °C and maintain a desulfurization rate of 100% after 6 cycles despite a slightly extended time. Notably, it can still efficiently remove DBT derivatives (such as BT and 4,6-DMDBT) in the same way that DBT is removed from fuel oil. This may be attributed to the W active sites with high electron density induced by abundant O$_V$ defects, the good dispersion and high exposure of the W sites, and the easy diffusion and contact between the substrate and active sites led by the spherical structure. The ODS reaction follows the HO$^{\bullet}$ radical mechanism. Overall, this research presents a controllable method for constructing heterogeneous SiW$_{12}$ with abundant O$_V$ defects, which could potentially expand its application in the deep ODS of fuel oils.

Data availability

Data for this article, including raw graphical data and ESI files, are available at Science Date Bank at **https://doi.org/10.57760/sciencedb.22886**.

Conflicts of interest

The authors report no declarations of interest.

Acknowledgements

References

1 J. Jiao, X. Zhou, S. Zhao, W. Jiao and R. Wang, *In situ* highly dispersed loading of molybdenum dioxide with oxygen vacancies on N-doped graphene for enhanced oxidative desulfurization of fuel oil, *J. Environ. Chem. Eng.*, 2023, **11**(2), 109402.

2 J. Zou, Y. Lin and C. Yang, Covalency triggers high catalytic activity of amorphous molybdenum oxides for oxidative desulfurization, *Sci. China: Chem.*, 2023, **66**(4), 1211–1220.

3 M. Yuan, H. Yuan, S. Xun, R. Le, Y. Huang, M. He, L. Zhu, W. Zhu and H. Li, VO_2 uniformly supported by 3D g-C_3N_4: A highly effective catalyst for deep oxidative desulfurization, *Fuel*, 2022, **319**, 123792.

4 J. Guo, L. Chu, H. Yang, Z. Huang, M. Yang and G. Wang, Amphiphilic halloysite nanotube enclosing molybdenum oxide as nanoreactor for efficient desulfurization of model fuels, *Chem. Eng. J.*, 2023, **451**, 138595.

5 X. Zhou, J. Jiao, W. Jiao and R. Wang, Oxidative desulfurization of model oil over the bowl-shaped N-doped carbon material loaded by the defective silicotungstic acid, *Sep. Purif. Technol.*, 2023, **310**, 123180.

6 G. Ye, Y. Gu, W. Zhou, W. Xu and Y. Sun, Synthesis of Defect-Rich Titanium Terephthalate with the Assistance of Acetic Acid for Room-Temperature Oxidative Desulfurization of Fuel Oil, *ACS Catal.*, 2020, **10**(3), 2384–2394.

7 M. O. Azeez and S. A. Ganiyu, Review of biomass derived-activated carbon for production of clean fuels by adsorptive desulfurization: Insights into processes, modifications, properties, and performances, *Arabian J. Chem.*, 2023, **16**(10), 105182.

8 J. Li, X. Jiang, M. Zhu and B. Dai, Cu(ı) anchoring in MOF-808 as a stable catalyst in ultra-deep oxidation desulfurization, *Fuel*, 2023, **341**, 127674.

9 J. Wang, B. Yang, X. Peng, Y. Ding, S. Yu, F. Zhang, L. Zhang, H. Wu and J. Guo, Design and preparation of polyoxometalate-based catalyst $[MIMPs]_3PMo_6W_6O_{40}$ and its application in deep oxidative desulfurization with excellent recycle performance and low molar O/S ratio, *Chem. Eng. J.*, 2022, **429**, 132446.

10 L. Hao, L. Sun, T. Su, D. Hao, W. Liao, C. Deng, W. Ren, Y. Zhang and H. Lü, Polyoxometalate-based ionic liquid catalyst with unprecedented activity and selectivity for oxidative desulfurization of diesel in [Omim]BF_4, *Chem. Eng. J.*, 2019, **358**, 419–426.

11 G. Zhang, F. Yang, W. Yang and Y. Li, N-doped carbon nanotube encapsulated nZVI as a high-performance bifunctional catalyst for oxidative desulfurization, *Particuology*, 2023, **81**, 109–118.

12 G. Ye, Y. Sun, D. Zhang, W. Zhou, C. Lancelot, A. Rives, C. Lamonier and W. Xu, Hierarchical porous titanium terephthalate based material with highly active sites for deep oxidative desulfurization, *Microporous Mesoporous Mater.*, 2018, **270**, 241–247.

13 R. Ghubayra, C. Nuttall, S. Hodgkiss, M. Craven, E. F. Kozhevnikova and I. V. Kozhevnikov, Oxidative desulfurization of model diesel fuel catalyzed by carbon-supported heteropoly acids, *Appl. Catal., B*, 2019, **253**, 309–316.

14 S. O. Ribeiro, D. Julião, L. Cunha-Silva, V. F. Domingues, R. Valença, J. C. Ribeiro, B. de Castro and S. S. Balula, Catalytic oxidative/extractive desulfurization of model and untreated diesel using hybrid based zinc-substituted polyoxometalates, *Fuel*, 2016, **166**, 268–275.

15 R. Wang, G. Zhang and H. Zhao, Polyoxometalate as effective catalyst for the deep desulfurization of diesel oil, *Catal. Today*, 2010, **149**(1–2), 117–121.

16 J. Kim, N. D. McNamara, T. H. Her and J. C. Hicks, Carbothermal reduction of Ti-modified IRMOF-3: an adaptable synthetic method to support catalytic nanoparticles on carbon, *ACS Appl. Mater. Interfaces*, 2013, **5**(21), 11479–11487.

17 X. Li, L. Zhang and Y. Sun, Titanium-modified MIL-101(Cr) derived titanium-chromium-oxide as highly efficient oxidative desulfurization catalyst, *Catalysts*, 2020, **10**(9), 1091.

18 L. Rivoira, M. L. Martínez, O. Anunziata and A. Beltramone, Vanadium oxide supported on mesoporous SBA-15 modified with Al and Ga as a highly active catalyst in the ODS of DBT, *Microporous Mesoporous Mater.*, 2017, **254**, 96–113.

19 X. Li, S. Huang, Q. Xu and Y. Yang, Preparation of WO_3-SBA-15 mesoporous molecular sieve and its performance as an oxidative desulfurization catalyst, *Transition Met. Chem.*, 2009, **34**(8), 943–947.

20 H. Yan, Y. Xie, Y. Jiao, A. Wu, C. Tian, X. Zhang, L. Wang and H. Fu, Holey Reduced Graphene Oxide Coupled with an Mo_2N–Mo_2C Heterojunction for Efficient Hydrogen Evolution, *Adv. Mater.*, 2017, **30**(2), 1704156.

21 N. A. Khan, B. N. Bhadra, S. W. Park, Y. Han and S. H. Jhung, Tungsten nitride, well-dispersed on porous carbon: remarkable catalyst, produced without addition of ammonia, for the oxidative desulfurization of liquid fuel, *Small*, 2020, **16**(12), 1901564.

22 F. Wang, Y. Liu, Y. Lv, J. Ren, R. Wang and W. Jiao, Oxidative desulfurization of liquid fuels catalyzed by $W_2C@C$ derived from metallophthalocyanine/phosphotungstic acid composites, *Sep. Purif. Technol.*, 2022, **281**, 119953.

23 P. Zuo, Y. Liu, J. Jiao, J. Ren, R. Wang and W. Jiao, Ultrafine W_2C well-dispersed on N-doped graphene: extraordinary catalyst for ultrafast oxidative desulfurization of high sulfur liquid fuels, *Appl. Catal., A*, 2022, **643**, 118791.

24 B. N. Bhadra, M. M. H. Mondol and S. H. Jhung, Metallic cobalt-anchored carbon with non-metallic heteroatom decoration: Remarkably effective oxidative desulfurization catalyst, *Sep. Purif. Technol.*, 2024, **330**, 125425.

25 Y. Liu, X. Yin, C. Li, Z. Xie, F. Zhao, J. Li, J. Hei, Y. Han, N. Wang and P. Zuo, Defective silicotungstic acid-loaded magnetic floral N-doped carbon microspheres for ultra-fast oxidative desulfurization of high sulfur liquid fuels, *Dalton Trans.*, 2023, **52**(46), 17524–17537.

26 Y. Liu, P. Zuo, R. Wang, Y. Liu and W. Jiao, Covalent immobilization of Dawson polyoxometalates on hairy particles and its catalytic properties for the oxidation

desulfurization of tetrahydrothiophene, *J. Cleaner Prod.*, 2020, **274**, 122774.

27 Y. Lv, J. Jiao, R. Wang and W. Jiao, Silicotungstic acid-supported C@SiO$_2$ nanospheres as an efficient oxidative desulfurization catalyst, *Chem. Eng. Sci.*, 2022, **248**, 117225.

28 E. A. Eseva, M. O. Lukashov, L. A. Kulikov, O. Y. Grafov, A. F. Bikbaeva and A. V. Akopyan, Transition to Carbon Materials: The Effect of Support Nature on the Catalytic Properties of Anderson-Type Polyoxometalate in Aerobic Oxidation of Sulfur-Containing Compounds, *Energy Fuels*, 2023, **37**(22), 17461–17472.

29 Y. Zhang and R. Wang, Synthesis of silica@C-dots/phosphotungstates core-shell microsphere for effective oxidative-adsorptive desulfurization of dibenzothiophene with less oxidant, *Appl. Catal., B*, 2018, **234**, 247–259.

30 J. Y. Qiu, F. H. Qin, B. Y. Xiao, M. T. Zhang, T. Wan, J. P. Liu, J. H. Chen and Z. Y. Huang, Surface-electronic-state-modulated, single-crystalline (001) alpha-Fe$_2$O$_3$ nanosheets with dual reaction sites for efficient fenton-like catalysis, *Chin. J. Inorg. Chem.*, 2019, **35**(9), 1665–1677.

31 C. Mao, H. Cheng, H. Tian, H. Li, W.-J. Xiao, H. Xu, J. Zhao and L. Zhang, Visible light driven selective oxidation of amines to imines with BiOCl: does oxygen vacancy concentration matter?, *Appl. Catal., B*, 2018, **228**, 87–96.

32 J. Zou, Y. Lin, S. Wu, Y. Zhong and C. Yang, Molybdenum dioxide nanoparticles anchored on nitrogen-doped carbon nanotubes as oxidative desulfurization catalysts: role of electron transfer in activity and reusability, *Adv. Funct. Mater.*, 2021, **31**(22), 2100442.

33 X. Chang, X. F. Yang, Y. Qiao, S. Wang, M. H. Zhang, J. Xu, D. H. Wang and X. H. Bu, Confined Heteropoly Blues in Defected Zr-MOF (Bottle Around Ship) for High-Efficiency Oxidative Desulfurization, *Small*, 2020, **16**(14), 1906432.

34 L. Ma, P. Wei, J. Li, X. Lu and G. Li, Preparation and catalysis of defected PVMo$_4$W$_7$@rht-MOF-1 for oxidation desulfurization under air, *Mol. Catal.*, 2024, **553**, 113784.

35 J. Sun, X. Ma, X. Li, J. Fan, Q. Chen, X. Liu and J. Pan, Synthesis of a cationic polyacrylamide under UV initiation and its flocculation in estrone removal, *Int. J. Polym. Sci.*, 2018, **2018**, 1–11.

36 Y. Sun, M. Ren, C. Zhu, Y. Xu, H. Zheng, X. Xiao, H. Wu, T. Xia and Z. You, UV-initiated graft copolymerization of cationic chitosan-based flocculants for treatment of zinc phosphate-contaminated wastewater, *Ind. Eng. Chem. Res.*, 2016, **55**(38), 10025–10035.

37 J. Ma, J. Shi, H. Ding, G. Zhu, K. Fu and X. Fu, Synthesis of cationic polyacrylamide by low-pressure UV initiation for turbidity water flocculation, *Chem. Eng. J.*, 2017, **312**, 20–29.

38 Y. Yu, D. Sun, S. Wang, M. Xiao, L. Sun and Y. Meng, Heteropolyacid salt catalysts for methanol conversion to hydrocarbons and dimethyl ether: effect of reaction temperature, *Catalysts*, 2019, **9**(4), 320.

39 Y. Chen, H.-y. Song, Y.-z. Lu, H. Meng, C.-x. Li, Z.-g. Lei and B.-h. Chen, Unified catalytic oxidation–adsorption desulfurization process using cumene hydroperoxide as oxidant and vanadate based polyionic liquid as catalyst and sorbent, *Ind. Eng. Chem. Res.*, 2016, **55**(39), 10394–10403.

40 J. Men, R. Wang, H. Li, X. Li, S. Yang, H. Liu and B. Gao, Preparation of crosslinked poly (acryloyloxyethyltrimethyl ammonium chloride) microsphere and its adsorption and mechanism towards shikimic acid, *Mater. Sci. Eng., C*, 2017, **71**, 167–175.

41 K. E. Lee, B. T. Poh, N. Morad and T. T. Teng, Synthesis and characterization of hydrophobically modified cationic acrylamide copolymer, *Int. J. Polym. Anal. Charact.*, 2008, **13**(2), 95–107.

42 H.-F. Pang, X. Xiang, Z.-J. Li, Y.-Q. Fu and X.-T. Zu, Hydrothermal synthesis and optical properties of hexagonal tungsten oxide nanocrystals assisted by ammonium tartrate, *Phys. Status Solidi A*, 2012, **209**(3), 537–544.

43 Y.-L. Zou, H.-Y. Li, W. Zhou, X.-G. Cui, G.-H. Zou and G.-Z. Shen, Introduction of the antibacterial drugs norfloxacin and Ciprofloxacin into a polyoxometalate structure: Synthesis, characterization, and antibacterial activity, *J. Mol. Struct.*, 2020, **1205**, 127584.

44 Z. Qi, Z. Huang, H. Wang, L. Li, C. Ye and T. Qiu, In situ bridging encapsulation of a carboxyl-functionalized phosphotungstic acid ionic liquid in UiO-66: a remarkable catalyst for oxidative desulfurization, *Chem. Eng. Sci.*, 2020, **225**, 115818.

45 S. Wang, X. Chen, Y. Tan, Z. Zhao, W. Yang, C. Huang, X. Wang, M. Chen, Z. Du and Y. Ding, Highly efficient synthesis of isoprene from methyl tert-butyl ether and formaldehyde over activated carbon supported silicotungstic acid catalysts, *Mol. Catal.*, 2020, **485**, 110840.

46 P. Wu, J. Yi, L. Feng, X. Li, Y. Chen, Z. Liu, S. Tian, S. Li, S. Khan and Y. Sun, Microwave assisted preparation and characterization of a chitosan based flocculant for the application and evaluation of sludge flocculation and dewatering, *Int. J. Biol. Macromol.*, 2020, **155**, 708–720.

47 N. Zhang, T. Zhou, M. Chen, H. Feng, R. Yuan, C. . a. Zhong, W. Yan, X. Tian, X. Wu, W. Chu, C. Wu and Y. Xie, High-purity pyrrole-type FeN$_4$ sites as a superior oxygen reduction electrocatalyst, *Energy Environ. Sci.*, 2020, **13**(1), 111–118.

48 T. Wang, X. Tang, S. Zhang, J. Zheng, H. Zheng and L. Fang, Roles of functional microbial flocculant in dyeing wastewater treatment: Bridging and adsorption, *J. Hazard. Mater.*, 2020, **384**, 121506.

49 K. Ye, K. Li, Y. Lu, Z. Guo, N. Ni, H. Liu, Y. Huang, H. Ji and P. Wang, An overview of advanced methods for the characterization of oxygen vacancies in materials, *TrAC, Trends Anal. Chem.*, 2019, **116**, 102–108.

50 Y. Ma, A. Li, C. Wang and X. Ge, Preparation of HPW@UiO-66 catalyst with defects and its application in oxidative desulfurization, *Chem. Eng. J.*, 2021, **404**, 127062.

51 A. Rajendran, H.-X. Fan, T.-Y. Cui, J. Feng and W.-Y. Li, Enrichment of polymeric WO$_x$ species in WO$_x$@SnO$_2$ catalysts for ultra-deep oxidative desulfurization of liquid fuels, *Fuel*, 2021, **290**, 120036.

52 Y. Du, L. Zhou, Z. Liu and L. Yang, Polyoxometalate-based 3DOM ZrO$_2$ material for deep oxidative desulfurization of

DBT with ultrahigh stability, *J. Porous Mater.*, 2020, **28**(1), 109–116.

53 Z. Ren, Q. Yuan, C. Dai and L. Zhu, Experimental and theoretical density functional theory approaches for desulfurization of dibenzothiophene from diesel fuel with imidazole-based heteropolyacid catalysts, *ACS Omega*, 2023, **8**(6), 5593–5606.

54 C. A. Virtudazo-Ligaray, M. D. G. de Luna, A. E. S. Choi and M. C. Lu, Novel cerium–tungsten–titanium-based catalyst for an efficient oxidative desulfurization material in fuel oil under a laboratory-scale setup, *Clean Technol. Environ. Policy*, 2023, **26**(4), 1135–1148.

55 M. Craven, D. Xiao, C. Kunstmann-Olsen, E. F. Kozhevnikova, F. Blanc, A. Steiner and I. V. Kozhevnikov, Oxidative desulfurization of diesel fuel catalyzed by polyoxometalate immobilized on phosphazene-functionalized silica, *Appl. Catal., B*, 2018, **231**, 82–91.

56 I. Shafiq, S. Shafique, P. Akhter, M. Ishaq, W. Yang and M. Hussain, Recent breakthroughs in deep aerobic oxidative desulfurization of petroleum refinery products, *J. Cleaner Prod.*, 2021, **294**, 125731.

57 W. Jiang, H. Jia, H. Li, L. Zhu, R. Tao, W. Zhu, H. Li and S. Dai, Boric acid-based ternary deep eutectic solvent for extraction and oxidative desulfurization of diesel fuel, *Green Chem.*, 2019, **21**(11), 3074–3080.

58 M. Y. Masoomi, M. Bagheri and A. Morsali, Application of two cobalt-based metal-organic frameworks as oxidative desulfurization catalysts, *Inorg. Chem.*, 2015, **54**(23), 11269–11275.